

Resolving the sodiation process in hard carbon anodes with nanostructure specific X-ray imaging

Martina Olsson¹, Antoine Klein¹, Nataliia Mozhzhukhina^{1,2}, Shizhao Xiong¹, Christian Appel³, Mads Carlsen³, Leonard Nielsen¹, Linnea Rensmo^{3,4}, Marianne Liebi^{1,3,4*}, Aleksandar Matic^{1*}

1. Department of Physics, Chalmers University of Technology Gothenburg 41296, Sweden.

2. SEEL Swedish Electric Transport Laboratory, Säve Flygplatsväg 27, 42373 Säve, Sweden

3. Center for Photon Science, Paul Scherrer Institut, 5232 Villigen PSI, Switzerland

4. Institute of Materials, Ecole Polytechnique Fédérale de Lausanne (EPFL), 1015 Lausanne, Switzerland

Abstract

Hard carbons show significant promise as anode materials for sodium-ion batteries. However, monitoring the sodiation process in the hard carbon electrode during cycling and understanding the sodiation mechanism remain challenging. This article reports on *operando* 2D scanning small- and wide-angle X-ray scattering (SWAXS) and *ex situ* 3D SAXS tomography of hard carbon electrodes during the sodiation process. Structural changes are monitored with spatial and temporal resolution during the electrochemical process and shows that sodiation through micropore filling is the more dominating mechanism in the later stages of sodiation, i.e. in the plateau region of the voltage profile, while intercalation occurs continuously. Spatial inhomogeneities are resolved over the electrode and reveal an increased level of inhomogeneity at higher degree of sodiation with regions of different degrees of micropore filling. Resolving the processes spatially enables us to correlate plating, starting from the interface between the electrode and the current collector, to a higher degree of micropore filling. The work demonstrates how SWAXS imaging can contribute to understanding the sodiation of hard carbon anodes, not only by spatially resolved analysis, but also as a method to decouple contributions from different components in a cell, enabling more accurate scattering analysis in *in situ* environments.

1. Introduction

Sodium-ion batteries present a sustainable alternative to lithium-ion batteries due to the significantly higher abundance of sodium compared to lithium^{1,2}. The sodium-ion battery is in many respects analogous to the lithium-ion battery in terms of configuration of the electrodes and electrolytes, simplifying the implementation and development towards the market. However, the graphite electrodes used in lithium-ion batteries are not suitable for sodium-ion batteries as sodium does not intercalate into graphite at ambient pressure^{3,4}. Hard carbon, a disordered carbonaceous material, is instead considered as the primary anode material^{5,6}. The structure of hard carbon consists of stacked graphene layers arranged in a non-uniform, chaotic manner forming microporous, granular particles. The precise structure of the hard carbon material will depend on both the precursor and the pyrolysis conditions, where in general a higher pyrolysis temperature results in a larger microporosity and decreased spacing between stacked graphene layers as well as decreased defect concentrations in the hard carbon matrix.⁷ This is reflected in a high diversity of structural features within the material class of hard carbons which contributes to the complexity to disentangle different sodiation mechanisms and a need for innovative characterization methods⁸.

A typical voltage profile of sodiation of hard carbon entails a sloping region at higher potentials (≈ 0.1 – 2.5 V vs Na/Na⁺) followed by a plateau region at lower potentials (≈ 0 – 0.1 V vs Na/Na⁺), Fig 1a. It has been proposed that sodiation in hard carbon occurs by several different mechanisms: edge and defect adsorption, intercalation, and micropore filling⁹⁻¹¹. However which mechanism determines the kinetics of sodiation in hard carbon, and which process is related to the different features in the electrochemical response, remains a question of controversy¹². However, there is an increasing preference that edge and defect adsorption and intercalation are dominating in the sloping region and micropore filling occurs in the plateau region^{8, 13-17}. In addition, unwanted sodium metal plating can occur in the hard carbon anode in the later stages of the electrochemical process which can lead to reduced capacity and cycle stability¹⁸. Due to the plateau region having a potential close to the one of sodium plating, this can be a serious concern particularly at high current rates¹⁹.

Small- and wide-angle X-ray scattering (SWAXS) have been extensively used to characterize carbonaceous materials as it provides insight into its nanostructure and molecular arrangement^{3, 13, 15, 20, 21}. For hard carbon SWAXS has been used to characterize structural changes from sodium insertion as the structural changes in the material revealed by the scattering signal can be related to a particular sodiation process and thereby reflect the sodiation mechanism^{15, 16, 20}. Furthermore, SWAXS is a useful method for *in situ* and *operando* studies of hard carbon, as shown by Stevens and Dahn¹⁶ and Iglesias et. al.¹⁵, enabling to directly monitor changes in the electrode structure during cycling. Following these temporally resolved SWAXS studies, we here apply exploit the capability of SWAXS imaging to study the sodiation of hard carbon with both temporal and spatial resolution to provide a new perspective for understanding the sodiation process. SWAXS imaging enables spatially resolved monitoring of structural changes during cycling which has recently been shown to reveal deformations in the interior of Li-ion batteries²². For sodiation of hard carbon, it can be applied to reveal inhomogeneities in the sodiation process over the anode. Spatial inhomogeneities in electrodes could lead to parts of the anode being underutilized, affecting the overall capacity and efficiency of the battery. Inhomogeneities in the degree of sodiation over the anode may also lead to localized failure, such as plating of metallic sodium or formation of cracks from localized stress and strain leading to mechanical degradation and loss of electrical conductivity. Furthermore, monitoring macroscopical inhomogeneities can provide information on the sodiation

mechanism e.g. by revealing kinetic limitations for the ionic and electronic transport in the electrode by gradients in the sodiation over the anode. In this work we use an approach where we with SWAXS imaging map a full hard carbon electrode in a half-cell in both 2D and 3D to spatially and temporally monitor structural changes during sodiation.

To enable SWAXS imaging of an electrode during cycling, we designed an electrochemical cell with a coated hard carbon electrode in a quartz capillary, Fig. 1a, Fig. S1a. In scanning SWAXS, images are collected by raster scanning the sample over a focused X-ray beam, building up a 2D grid where in each position the scattering pattern of the sample is recorded, Fig. 1b, c. From the scattering signal, images can be extracted with the specific contrast originating from a particular scattering feature mapped in each pixel, e.g., the scattering intensity in a chosen q-region. With the high flux offered by synchrotron sources, each scattering pattern is collected within 0.1s, enabling time resolved measurements and a 2D mapping of the full electrode ($1.5 \times 0.3 \text{ mm}^2$) with a pixel resolution of $15 \times 25 \text{ }\mu\text{m}^2$ within a few minutes.

In SAXS tomography, multiple 2D images are collected at different projection angles between 0° and 180° , Fig. 1d, to generate a 3D mapping of the electrode. From the projection images, the scattering of the full electrode volume is reconstructed, generating volumes where each voxel contains the reconstructed scattering signal in that position. This enables both an exact evaluation of the scattering from a specific part of the electrode and from a localized volume of material, with a volume given by the size of the X-ray beam. In this way, SAXS tomography can distinguish between scattering coming from the electrode and from the rest of the cell, enabling a more accurate evaluation of the scattering compared to 2D measurements, with the downside of longer measurement time, on the time scale of a few hours for a tomography compared to 10 minutes for a similar electrode volume with the same pixel resolution.

In this study we use a combination of *operando* 2D scanning SWAXS and *ex situ* 3D SAXS tomography to spatially resolve structural changes in hard carbon electrodes during sodiation and correlate this to the suggested mechanisms of sodiation. *Operando* 2D scanning SWAXS was performed to image the electrode in real time and follow the progression of micropore filling, intercalation and plating over the electrode. Correlating the structural changes with the electrochemistry of the cell suggests that micropore filling is dominating in the plateau region of the voltage profile, while intercalation between stacked graphene layers contribute throughout the full sodiation process. Sodium metal plating is identified in the later stages of the electrochemical process and appears to start growing from the interface of the electrode and the current collector. *Ex situ* 3D SAXS tomography was performed to obtain volume resolved scattering data. With tomography, two *ex situ* cells cycled to different degrees of sodiation were imaged, revealing a higher level of spatial inhomogeneity in the degree of microporosity filling over the electrode at higher degree of sodiation. This demonstrates how SWAXS imaging can provide new insight in the sodiation process of hard carbon anodes for sodium-ion batteries.

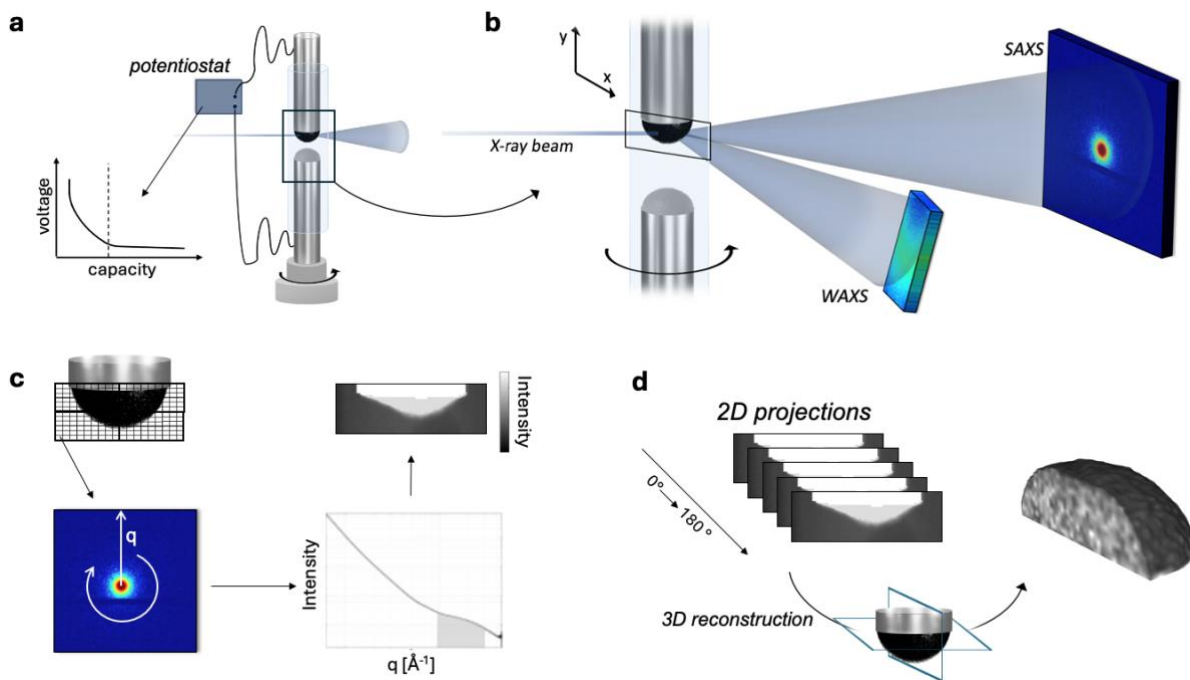


Figure 1. Schematic of SWAXS imaging of a hard carbon electrode **a)** An electrochemical sodium-ion cell is built in a quartz capillary. The cell is positioned on translational and rotational stages, illuminated with a focused X-ray beam and connected to a potentiostat to enable *operando* experiments. **b)** For each illuminated position, a 2D detector image is recorded on a SAXS detector placed 2 m downstream of the sample and a WAXS detector placed below the sample at a distance of 0.6 m, capturing the q -range corresponding to the characteristic scattering properties of hard carbon. **c)** To create a 2D image of the electrode, the sample is raster scanned through the beam, creating a projection of the electrode where each pixel contains the information of the scattering properties in that position. The detector images are azimuthally integrated to retrieve the 1D scattering curves in each pixel. Images of the electrode can then be created by using the scattering intensity in different q -regions as the grey scale of the image. **d)** To perform 3D imaging, the same data acquisition as for the 2D images are applied but from multiple rotation angles to build up a stack of projection images around the sample. These projections can then be used to reconstruct back a 3D volume of the scattering intensity in different q -regions and ultimately produce a 4D volume where the scattering in each voxel position is resolved. To visualize the spatial analysis, the scattering properties in a specific q -region can be selected to create a grey scale contrast in the volume.

Result and discussion

2. Structural characterization of the hard carbon anode

Figure 2 shows the SWAXS scattering curve from the pristine hard carbon powder used as active material in the electrodes. The curve displays the characteristic signal from disordered, microporous carbon which can be divided in three main scattering contributions: a q^{-4} slope from surface scattering of particles in the low q -region ($< 0.1 \text{ \AA}^{-1}$), a shoulder ($\sim 0.1 - 0.5 \text{ \AA}^{-1}$) from microporosity, and a broad amorphous peak ($\sim 1.6 - 1.7 \text{ \AA}^{-1}$) from the interatomic scattering of stacked graphene layers referred to as the 002-peak of hard carbon, consistent with the interlayer spacing 002-peak that is observed in graphite^{3, 23}. These scattering signals will change depending on how the carbon structure is affected by the different sodiation mechanisms^{15, 16, 20}. Sodiation through micropore filling will affect the intensity and shape of the shoulder in the mid- q region^{15, 16, 20}. This shoulder results from the electron density difference between pores and the carbon matrix. If sodium is entering the pores, the electron density difference will decrease, leading to a decrease in scattering intensity in this region¹⁵. For sodium intercalation an increase in the average interlayer spacing between the graphene layers is expected. As the interlayer spacing is inversely related to the peak position of the 002-peak through Bragg's law ($d=2\pi/q^*$) a decrease in peak position illustrates an increase in interlayer distance^{20, 23}. A decrease in peak intensity can be correlated to the presence of scattering species between the carbon layers which scatter X-rays out of phase with the layers causing destructive interference²³. Sodium metal plating would result in the appearance of a diffraction peak from metallic sodium at 2.07 \AA^{-1} ²⁰. The process of adsorption on defects and surfaces are difficult to directly link to a specific change in scattering curve from hard carbon as sodium is assumed to be adsorbed both at defects on edges of graphene sheets and on surfaces of the graphene layers within the micropores. It can therefore be expected that these processes may induce a slight decrease in the intensity of both the microporous region as well as in the intensity of the 002-peak in the carbon structure from destructive interference from adsorbed sodium on the surfaces of the 002 planes^{23, 24}.

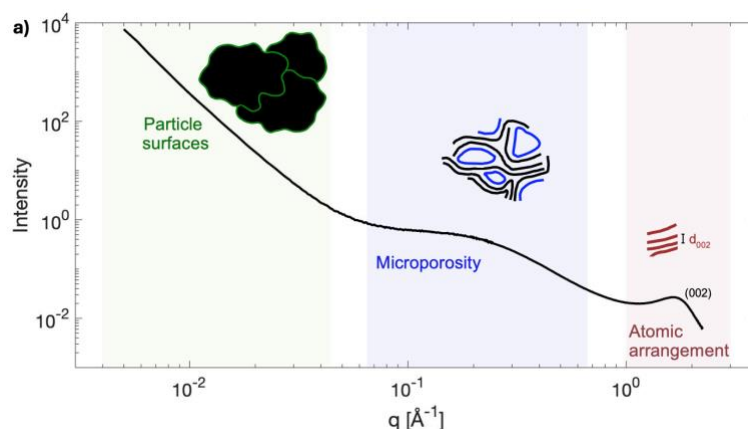


Figure 2. Structure of the active hard carbon material. Combined SAXS and WAXS profile of the hard carbon powder used in the hard carbon anodes, demonstrating the characteristic scattering curve of hard carbon with the three characteristic structural regions highlighted. Schematic visualization inspired by Saurel et al.³

For performing a spatial SAXS analysis of the sodiation of hard carbon electrodes a SAXS tomography measurement was first performed on a pristine hard carbon electrode, the inactive binder material. The electrode was placed in the electrochemical cell to validate the method and to evaluate the homogeneity of a non-sodiated electrode. Figure 3a shows SAXS curves extracted from a few positions marked Figure 3b to exemplify the scattering signal at different

positions. Figure 3b shows two horizontal 2D slices extracted from the tomogram volume with a grayscale of the scattering intensity at $q = 0.1 - 0.5 \text{ \AA}^{-1}$ corresponding to scattering from the microporosity in the hard carbon and at $q = 0.075 \text{ \AA}^{-1}$ where small inhomogeneities are found across the anode. This scattering contribution is attributed to the binder in the electrode, as supported by previous work showing that the decaying slope from the binder gives an additional scattering contribution at low q ²⁵. The scattering intensity in the microporous region shows a high homogeneity over the anode, thus the distribution of hard carbon over the electrode. Figure 3c visualizes a 3D rendering of the electrode derived from the scattering intensity in the microporous region, illustrating the spherical cap shape of the dip coated electrode.

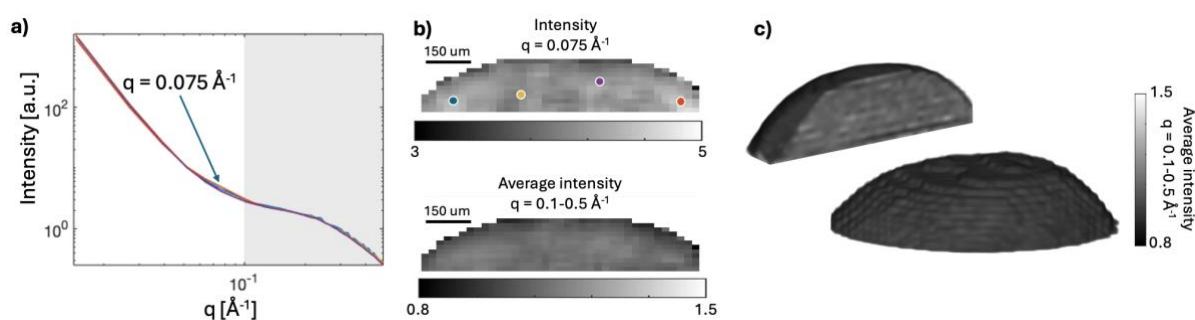


Figure 3. Spatially resolved scattering of a pristine hard carbon electrode. a) SAXS curves reconstructed for the spatial positions marked in b. b) 2D slices extracted from the tomogram with the scattering intensity at $q = 0.075 \text{ \AA}^{-1}$ and $q = 0.1 - 0.5 \text{ \AA}^{-1}$ c) 3D visualization of a hard carbon electrode reconstructed by the scattering intensity in the q -region corresponding to the microporous region. The images display the full electrode and a cross-sectional view of the interior.

3. *Operando* 2D SWAXS imaging of the sodiation process

Figures 4 - 8 show results from the *operando* 2D scanning SWAXS experiment of a hard carbon electrode during galvanostatic sodiation. The voltage profile, Fig. 4a, shows a rapid voltage decrease in the sloping region followed by a plateau region. After about 50 min a decrease in voltage is observed indicating the onset of sodium plating. The cell was sodiated with a current of $14 \mu\text{A}$ resulting in an applied discharge rate (C-rate) of 0.8C which corresponds to a current density of 0.23 A/g , based on the estimated mass of the electrode. Calculations are found in the supporting information, Table S1. The cell is a two-electrode cell, and its geometry creates a high internal resistance which contributes to a higher over voltage. This causes a shift of the voltage recorded and the plateau region to appear to have a negative voltage. *Operando* scanning SWAXS images were recorded every 10 min, marked in grey in the voltage profile. Figure 4b shows the averaged scattering intensity over the q -region $q = 0.06 - 0.5 \text{ \AA}^{-1}$, corresponding to the microporous region. Over the first hour of sodiation, the morphology of the electrode is unchanged, as seen by the homogeneous intensity distribution, but in the later stages the intensity distribution becomes progressively more inhomogeneous and the shape of the electrode changes. This coincides with the onset of sodium plating from op 5 see further below, after which the electrode swells and deforms (op 7) and finally starts to delaminate (post).

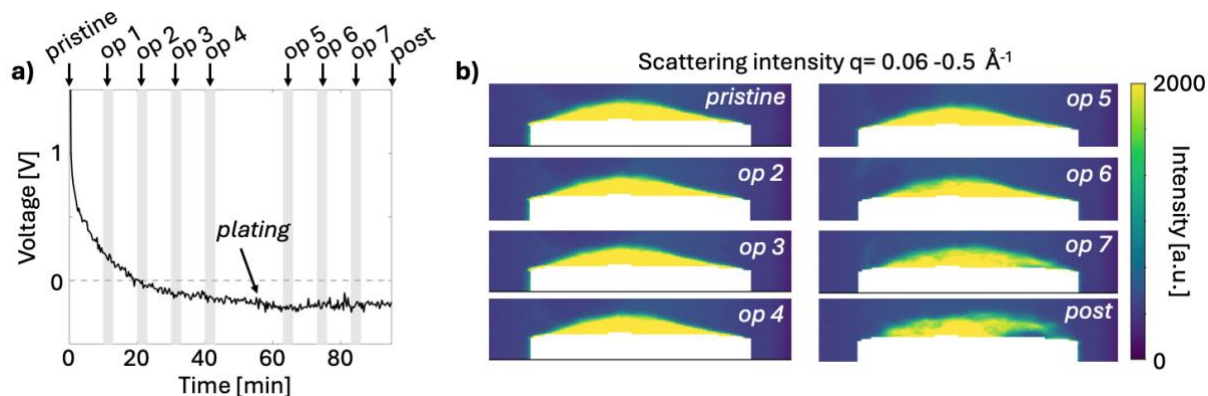


Figure 4. Operando 2D SWAXS imaging of the electrode a) Galvanostatic voltage profile of the sodiation of the hard carbon electrode. The cell is cycled with a current of $14 \mu\text{A}$ corresponding to an estimated C-rate of 0.8C. Grey lines indicate points of collection of scanning SWAXS images during the *operando* experiment (op #). b) Scanning SWAXS images of the averaged intensity in the q -region ($q = 0.06 - 0.5 \text{ \AA}^{-1}$) where hard carbon scatters strongly and the electrode appears bright. The current collector is masked in white.

Figure 5a shows the SAXS curves where the intensity has been averaged over the full projected area of the electrode for the first five *operando* scans. The SAXS curves display the characteristic scattering features of hard carbon and an additional contribution around $q = 0.075 \text{ \AA}^{-1}$. This contribution is attributed to the inactive materials in the electrode, including the binder and remains stable during cycling and does not affect the analysis of structural changes in the hard carbon during sodiation evaluated in the experiment. Two main changes are observed in the SAXS signal during sodiation. A decrease in intensity in the microporous region ($q = 0.12 - 0.4 \text{ \AA}^{-1}$), and an increase in intensity in the particle surface region ($q = 0.0045 - 0.007 \text{ \AA}^{-1}$), Figure 5a grey highlighted regions. The time evolution of the average intensities in these two q -regions is shown in Figures 5b. Initially, the intensity in the microporous region increases slightly followed by a pronounced decrease in intensity. The initial increase has been suggested to be related to an increased density difference between pores and the carbon matrix due to sodium intercalation¹⁵ and the change implies that sodium first start to intercalate into the carbon structure. As the sodiation progresses further, the intensity decreases, indicating a decreased density difference between pores and carbon matrix, suggesting filling of micropores with sodium. When the electrochemical profile reaches the plateau region, the intensity decreases more rapidly reflecting that pore filling is now the dominating mechanism, in agreement with previous reports in literature^{8, 13-17}.

In the low- q region related to scattering from the hard carbon particles surface, the intensity increases continuously during sodiation however more rapidly initially, Fig. 7b. This increase is less straightforward to directly correlate to a sodiation mechanisms and is more likely related to the formation of a solid electrolyte interphase (SEI) on the surface of the particles which is formed by decomposition products from the electrolyte. The more rapid initial intensity increase is consistent with SEI formation which is formed at higher voltages in the initial stages of sodiation¹⁴.

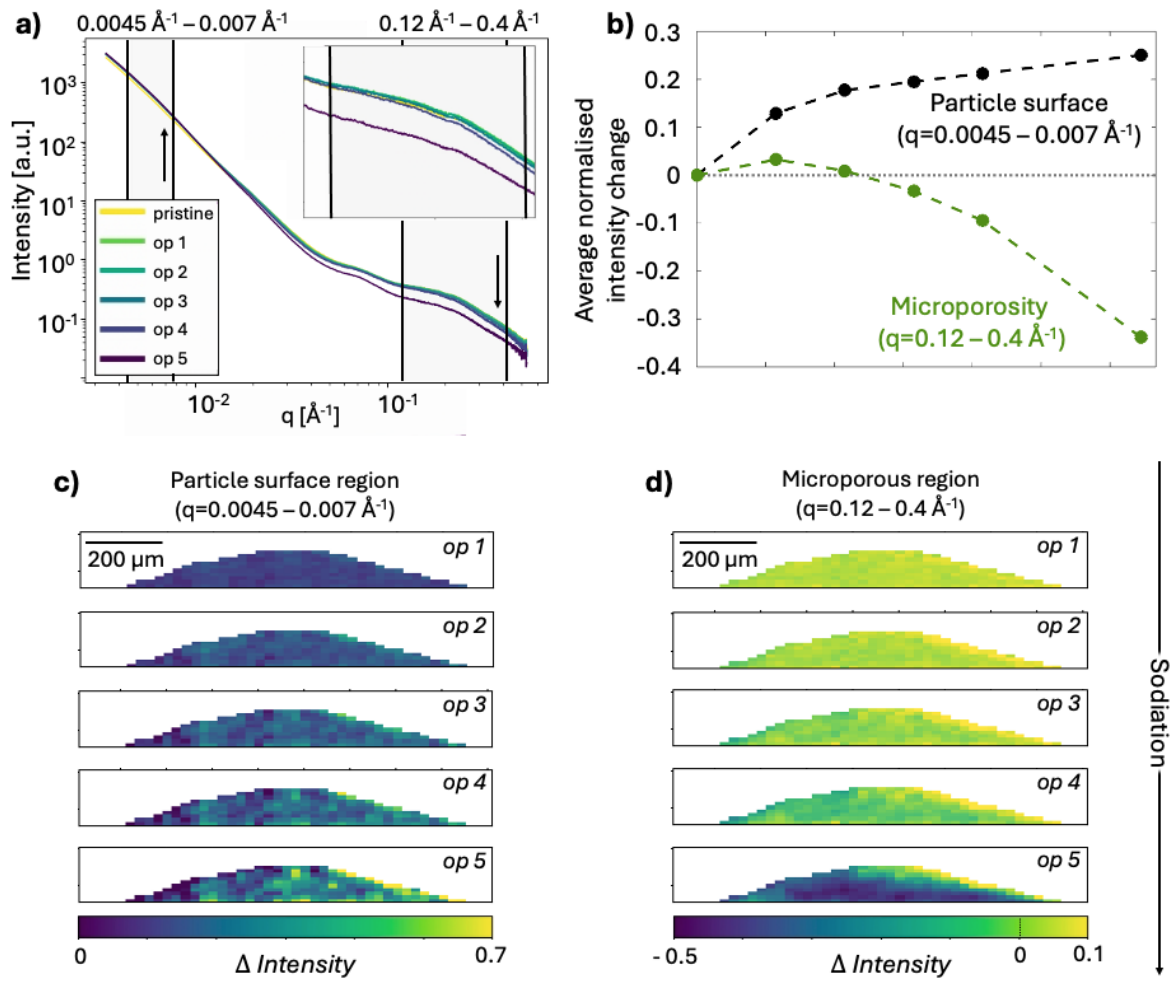


Figure 5. Structural changes in the SAXS region. a) SAXS curves of the averaged intensity over the full projected area of the electrode for the first five operando scans. Inset shows a magnified view of the q -range corresponding to scattering from micropores. The selected q -ranges representing the characteristic q -region are marked by black lines. b) Line plot of the changes in intensity in the selected q -ranges (marked by black lines in a) during the electrochemical process averaged over the full electrode. c) Difference maps of the integrated intensity in the particle surface region ($0.0045 - 0.007 \text{ \AA}^{-1}$) and d) microporous region ($0.12 - 0.4 \text{ \AA}^{-1}$). Difference maps are created by subtracting the intensity of the pristine scan from the *operando* scan followed by division by the intensity of the pristine electrode, to normalize the signal from thickness variations over the electrode and highlight changes in intensity in each pixel. The intensity of electrolyte surrounding the electrode is masked out.

Figures 5c,d show scanning SAXS images of the scattering intensity in the microporous ($q = 0.12 - 0.4 \text{ \AA}^{-1}$) and particle surface ($q = 0.0045 - 0.007 \text{ \AA}^{-1}$) regions, respectively. The 2D images are displayed as difference maps between the intensity in the selected q -regions of the *operando* image (op #) and in the pristine image, according to equation 1. The difference maps are created by subtracting the average intensity in the selected q -region of the pristine electrode from the intensity in the *operando* scans in each pixel and normalizing by the intensity from the pristine electrode, to emphasize the differences during sodiation and correct for thickness variations in the 2D projections. Figure S2 shows how the scattering curves change at a few selected points in the sample.

$$\text{Difference map} = \frac{\bar{I}_{op\#}^{\text{selected } q\text{-region}} - \bar{I}_{pristine}^{\text{selected } q\text{-region}}}{\bar{I}_{pristine}^{\text{selected } q\text{-region}}} \quad \text{eq. 1.}$$

During sodiation, the intensity in the microporous region first increases rather homogeneously over the electrode (op 1 and 2 in Fig. 5d). As the sodiation process continues (op 3-5), inhomogeneities arise and a decreased intensity can be observed over almost the entire electrode. In particular, the region close to the current collector shows a clear intensity decrease, indicating a higher degree of pore filling occurring in this part of the electrode. A larger degree of sodiation close to the current collector indicates that the electrode does not experience ion-depletion, which would be expected to result in the opposite gradient with a higher degree of sodiation close to the surface of the electrode and the electrolyte. The radial gradient with higher degree of sodiation closer to the current collector can instead be a result of a low electronic conductivity in the electrode leading to faster kinetics closer to the current collector. In the particle surface region, an increased inhomogeneity in the intensity difference is also observed throughout the sodiation process. The spatial changes in this region appear not to be correlated with the spatial changes in the microporous region, suggesting that the origins of the structural changes are not correlated.

Figure 6a shows the WAXS curves where the intensity has been averaged over the full projected area of the electrode for the first five *operando* scans. The WAXS curve contains the scattering signal from the broad 002-peak from hard carbon as well as a peak at $q = 1.45 \text{ \AA}^{-1}$ attributed to the binder, Fig S3. During sodiation the 002-peak both decreases in intensity and the peak position shifts to lower q -values, which both are indicators for sodium intercalation²⁰. The peak position in each scan was determined by a gaussian fit and can be used to calculate an average interlayer spacing in each point from Braggs law ($d=2\pi/q^*$), Fig S4, Table S2. A continuous change in intensity and interlayer spacing is observed throughout the sodiation process, Figure 6B, supporting the SAXS results that intercalation occurs early in the sodiation process but also show that intercalation continuous also throughout the plateau region. In the fifth *operando* scan (op 5), a broad contribution at $q = 2.0 - 2.3 \text{ \AA}^{-1}$ appears which can be related to the formation of pseudo-metallic sodium²⁰, resulting from extensive micropore filling with confined Na clusters in the micropores^{20, 26}. Figure 6c shows the difference map of the integrated intensity of the 002-peak over the electrode. The signal to noise ratio is rather low in each pixel in this q -range due to the strong background from the electrolyte, but a slightly larger decrease in intensity can be observed in the outer left part of the electrode as well as closer to the current collector. This agrees with the observations made from the microporous region in SAXS showing that a larger fraction of micropores is filled closer to the current collector which could indicate a low electronic conductivity in the bulk electrode.

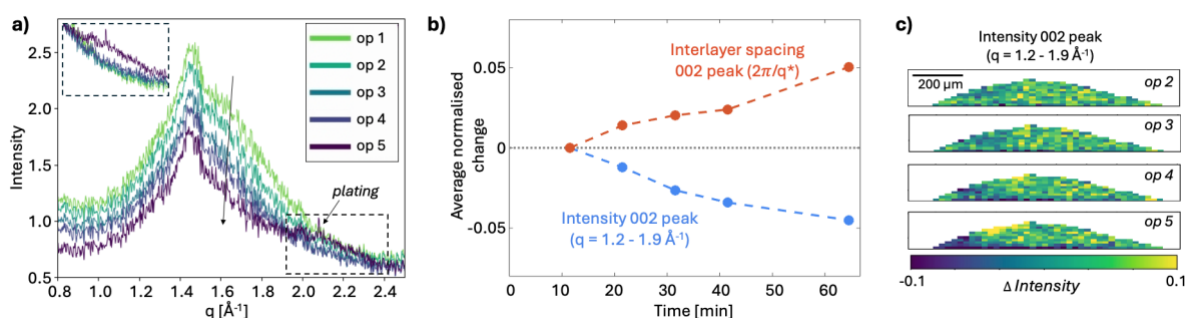


Figure 6. Structural changes in the WAXS region a) WAXS curves of the averaged intensity over the full projected area of the electrode for the first five *operando* scans. Inset shows the curves normalized for the change in intensity of the 002-peak revealing a contribution from pseudo-metallic sodium in the range $q = 2.0 - 2.3 \text{ \AA}^{-1}$ appearing in the 5th *operando* scan. b) Line plot of the changes in intensity in the q -range of the 002-peak ($q = 1.2 - 1.9 \text{ \AA}^{-1}$) and the average interlayer spacing of graphene layers derived from the 002-peak position. c) Difference map of averaged intensity of the 002-peak ($q = 1.2 - 1.9 \text{ \AA}^{-1}$). The intensity of electrolyte surrounding the electrode is masked out.

Figure 7a shows the difference map of the intensity of the q-region with the broad peak from Na-Na correlation ($q = 2.0 - 2.3 \text{ \AA}^{-1}$) where a high intensity indicates a presence of pseudo-metallic sodium in the pores. Similar to the SAXS results the highest signal is shown close to the current collector, indicating extensive pore filling in this region of the electrode. Figure 7b shows a scatter plot of the intensity difference in each pixel of the electrode within the WAXS region for pseudo-metallic sodium (y-axis) and the SAXS region for microporosity filling (x-axis). The plot visualizes how the higher contribution of the broad WAXS peak appears where there is also a low intensity in the SAXS microporous region (top left) which shows that the micropores indeed are extensively filled at the onset of formation of pseudo-metallic sodium.

Figure 7c-d shows an overview of the changes observed in the electrode during sodiation by a combined plot of the normalized changes in intensity in the different q-regions corresponding to the different sodiation processes, Fig 7d, together with the electrochemical profile of the cell, Fig 7c. The results visualize how the intensity and derived interlayer spacing of the 002-peak, related to sodium intercalation, changes continuously during the electrochemical process whereas the scattering related to micropores in the carbon matrix decreases faster in the plateau region in the later stages of sodiation. This indicates that filling of microporosities dominates in the later stages of the electrochemical process which is also supported by the appearance of a peak for pseudo-metallic sodium in the fifth operando scan, Fig 6.

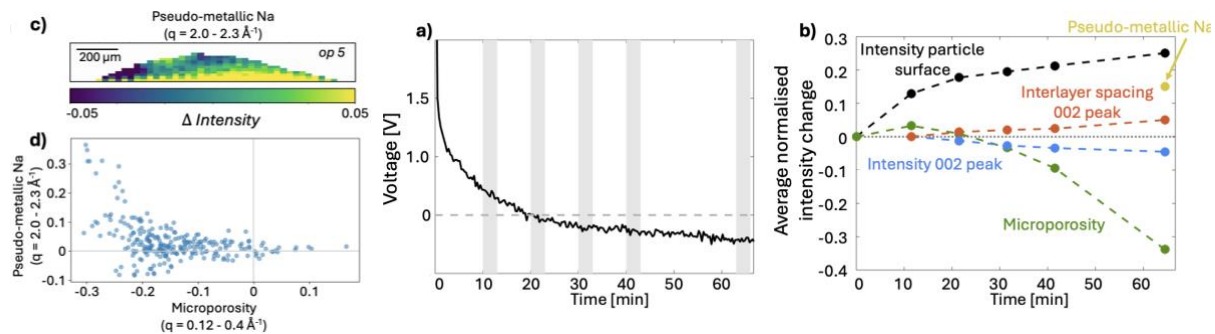


Figure 7. Overview of the changes in scattering signal over the electrode during sodiation **a)** Difference map of the average intensity in the q-region of pseudo-metallic sodium ($q = 2.0 - 2.3 \text{ \AA}^{-1}$). **b)** Comparison of the intensity change in the q-regions related to microporosity filling from SAXS (x-axis, $q = 0.12 - 0.4 \text{ \AA}^{-1}$) and WAXS (y-axis, ($q = 2.0 - 2.3 \text{ \AA}^{-1}$)). **a)** Voltage profile of the sodiation process of the first 60 min before excessive sodium plating **b)** Overlay of the line plots of the average intensity in selected q-regions corresponding to the different mechanisms of sodiation during the electrochemical process. The plot visualizes the changes in the particle surface region, $q = 0.0045 - 0.007 \text{ \AA}^{-1}$ (black), microporous region $q = 0.12 - 0.4 \text{ \AA}^{-1}$ (green) and the 002-peak $q = 1.2 - 1.9 \text{ \AA}^{-1}$ (blue) as well as the change in average interlayer spacing of graphene layers (orange). The appearance of pseudo-metallic sodium, $q = 2.0 - 2.3 \text{ \AA}^{-1}$, after 60 min is illustrated by the yellow marker.

After 65 min (op 5), signatures of Na-plating can be detected in the WAXS curve by the appearance of a diffraction peak at 2.08 \AA^{-1} from metallic sodium, Fig. 8a. Figure 8b shows the spatial distribution of the intensity corresponding to the diffraction peak over the electrode, where a yellow color indicates a presence of metallic sodium. The plating starts close to the current collector and progressively grows from the bottom of the electrode. The excessive plating in the last scans can be correlated to the swelling, deformation and delamination of the electrode from the current collector observed in Fig. 4b. These results demonstrate a clear preference of plating to occur first close to the current collector where one also observes a higher degree of micropore filling. The high degree of pore filling eventually results in the formation of pseudo-metallic sodium in the micropores that can act as a precursor to development of sodium plating close to the current collector.

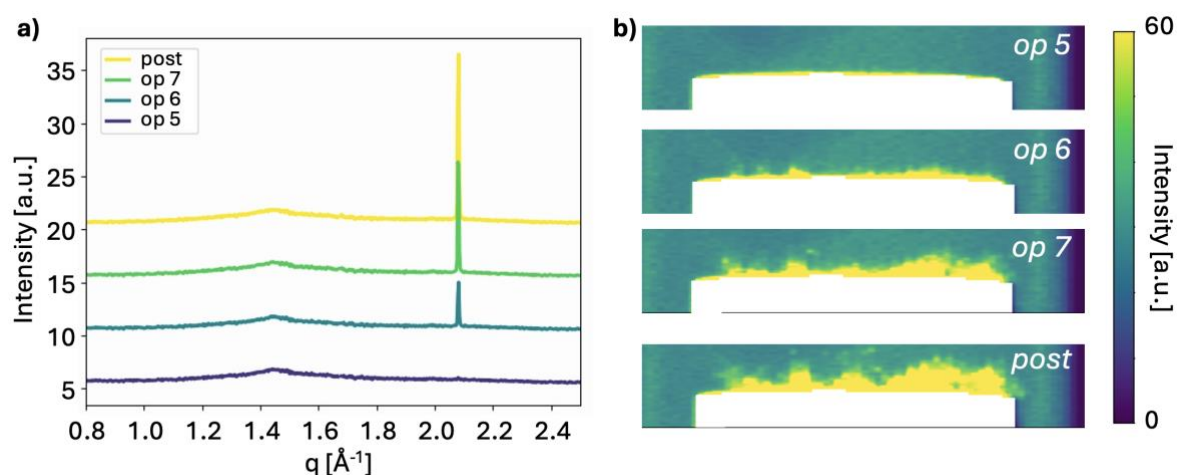


Figure 8. Spatial and temporal progression of sodium plating in the electrode a) Average WAXS curves of the electrode in the later stages of sodiation of the electrode (op 5-7, post), offset for visibility. b) Scanning WAXS images of the intensity distribution of the peak for metallic sodium (2.08 \AA^{-1}), sodium plating corresponds to a high intensity. The current collector is masked in white.

4. 3D SAXS tomography of sodiated electrodes

To analyze electrodes with volume resolved scattering, SAXS tomography was performed on two sodiated electrodes. Due to the long acquisition time for a tomogram, 3D SAXS analysis was not compatible with operando measurements due to its need for time-resolution and were instead performed on *ex situ* samples. The *ex situ* samples were extracted from two different cells cycled to different degree of sodiation. For the first electrode, sodiation was stopped in the first sloping region (100 min) whereas for the second electrode sodiation was stopped far in the plateau region (200 min), Figure 9a. These two cases will further on be referred to as the electrode of low and high degree of sodiation and be compared to the pristine electrode, Figure 3. The electrodes were cycled with an estimated C-rate of 0.3C and 0.2C for the samples with low and high degree of sodiation, respectively, Table S1.

Figure 9 provides an overview of the features observed from SAXS tomography. Figures 9b, c shows scattering curves from two selected voxels for each sample to exemplify the scattering from the two different electrodes. The average scattering curve from the pristine electrode is included for comparison (black curves) to emphasize the differences in scattering as a result of sodiation. As expected, the intensity in the microporous region ($0.2 - 0.5 \text{ \AA}^{-1}$), characteristic for pore filling, decreases with an increasing degree of sodiation. A decrease in slope in the low q -region is found for both electrodes, and an increased intensity contribution around 0.075 \AA^{-1} is found in the electrode with a high degree of sodiation. The contribution at 0.075 \AA^{-1} is here most likely due to SEI formation on the surface of the hard carbon particles as well as residues of salt and electrolyte in the *ex-situ* cells which can create particles on the surface of the electrode on that length scale.

To evaluate spatial inhomogeneities of the sodiation from pore filling Figures 9d-f show 2D slices of the integrated intensity in the microporous region ($0.2 - 0.5 \text{ \AA}^{-1}$) extracted horizontally and vertically from the center of the tomograms. As each voxel contains the scattering signal from a defined amount of material, the scattering intensity is directly comparable between voxels and between the different samples. The pristine sample, Figure 9d, therefore serves as a reference for the intensity distribution and homogeneity of a hard carbon electrode. The

sodiated samples show a decreased intensity in the microporous region, as well as an increased inhomogeneity in the intensity distribution over the electrode. Figure 9g displays the histograms of the averaged intensity in the q -region $0.2\text{\AA}^{-1} - 0.5\text{\AA}^{-1}$ in each pixel, in the three different electrode volumes. The sodiated electrodes both show a decreased intensity, suggesting that some pore filling already occurs at low degree of sodiation, within the sloping voltage profile. One explanation to the presence of sodium in the micropores in the sample sodiated to a low degree of sodiation could be that adsorption on defects within the pores occur in the early stage of sodiation and may therefore also affect the scattering intensity in this q -range. With increased degree of sodiation, the average intensity decreases further, and the width of the histogram increases, illustrating the increased inhomogeneity in micropore filling in the highly sodiated electrode.

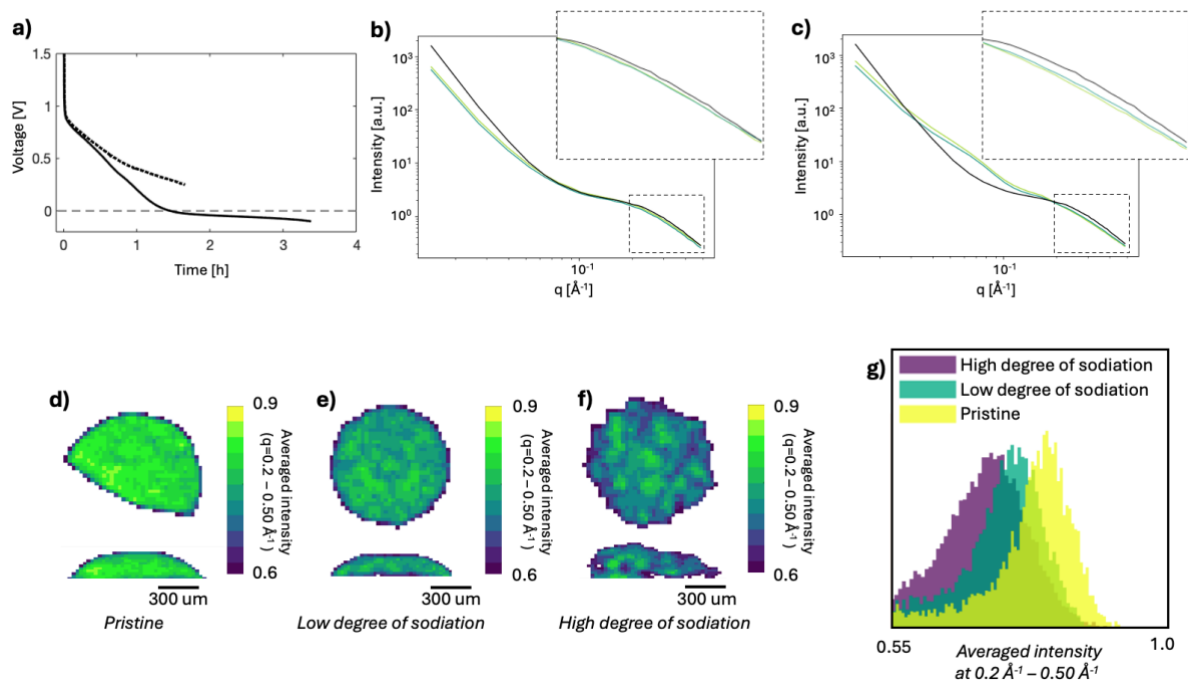


Figure 9. *ex situ* 3D SAXS tomography of hard carbon electrodes. **a)** Voltage profile of the *ex-situ* cells with low degree of sodiation (dashed line) and high degree of sodiation (full line) discharged with an estimated C-rate of 0.3C for 100 min and 0.2C for 200 min, respectively. SAXS curves in a few selected voxels in the electrode with **b)** low degree of sodiation and **c)** high degree of sodiation. The reference to the scattering intensity of the pristine electrode is shown in black. 2D slices extracted horizontally and vertically from the tomograms of the integrated intensity in the microporous region ($0.2 - 0.5 \text{ \AA}^{-1}$) of the **d)** pristine hard carbon electrode, **e)** the electrode with low degree of sodiation and **f)** the electrode with high degree of sodiation. **g)** Histograms of the integrated intensity of the microporous q -region for the three electrodes. Due to the outer voxels at the electrode surface being only partly filled with electrode, a lower intensity value is observed here which is reflected in the tails of the histogram and is not related to the sodiation process but rather the shape of the electrode.

5. Conclusion

In this paper we demonstrate SWAXS imaging as a characterization method to in detail investigate the mechanisms of sodiation of hard carbon electrodes. By imaging the local scattering signal over the hard carbon anode, structural changes are spatially resolved and correlated to the mechanisms of sodiation and the electrochemical process. With scanning SWAXS, we perform *operando* 2D imaging of a hard carbon anode during sodiation, monitoring the structure in real time. This reveals that sodiation through micropore filling is the more dominating mechanism in the later stages of sodiation, while intercalation occurs

continuously during sodiation. Plating is shown to initiate from the interface of the electrode and current collector where also a higher degree of micropore filling is found. With SAXS tomography, we image the scattering in the anode in 3D, revealing an increased level of inhomogeneity at a higher degree of sodiation with regions of different degrees of micropore filling.

The application of SWAXS imaging presents opportunities for detailed studies of the sodiation in hard carbon anodes, not only by spatially resolved analysis, but also as a method for decoupling the contributions of different components in a cell, enabling more accurate scattering analysis in *in situ* environments. By using a multiscale imaging approach, SWAXS imaging enables mapping of structural changes during charging to reveal microscopic heterogeneities which can give insights into the functionality and failure mechanism of Na-ion batteries. Thus, our approach paves way for a deeper understanding of the storage mechanism in hard carbon anodes.

Methods

Electrochemical cell preparation

A dedicated electrochemical cell for *operando* SWAXS imaging was built using a quartz capillary with an internal diameter of 1.5 mm and wall thickness of 150 μm . Quartz capillaries were used to minimize the SAXS scattering background. Stainless steel pins were used as current collectors, polished to obtain a flat substrate, and the hard carbon electrode was prepared by dip coating the flat tip of the stainless-steel pin in a hard carbon slurry and dried at 80 $^{\circ}\text{C}$ in vacuum overnight. The slurry was made of 85 wt.% hard carbon (Kureha Battery Materials Japan), 10 wt.% polyvinylidene fluoride (PVDF) binder (Sigma Aldrich) and 5 wt.% carbon additives (Carbon black Super P[®], ThermoFisher), dispersed in N-methyl-2-pyrrolidone (NMP), (Sigma Aldrich). The cell was assembled by inserting the pin with the coated hard carbon electrode, filling it with electrolyte, 1M NaPF₆ in EC: PC (Ethylene carbonate: Propylene carbonate) 1:1 by weight (E-Lyte Innovation), and inserting a pin with Na metal (dry stick, Thermo scientific chemicals) attached to it as counter electrode in the glass capillary. The cell was sealed with UV-curable glue. Schematics and photographic images of the cell are shown in Figure S1. The dip coating resulted in a variation in mass between electrodes below the accuracy of the scale and the mass of active material (hard carbon) was instead calculated based on the volume determined from SWAXS imaging and the composition of the slurry and the density of hard carbon. The calculations are shown in the supporting information. From the mass of active material an applied C-rate of approximately 0.8C was estimated for the *operando* cell, while for the *ex situ* cells a C-rate of 0.3C and 0.2C was estimated for the electrodes cycled to a low and high degree of sodiation, respectively (Table S1). For *ex situ* tomography experiments the pin with the hard carbon electrode was transferred to an empty capillary to remove the excess scattering and absorption of the electrolyte.

SWAXS and SAXS imaging measurement

SWAXS patterns of the pristine hard carbon powder was measured with a Mat: Nordic X-Ray scattering instrument (SAXSLAB) equipped with a high brilliance Rigaku 003 X-Ray micro-focus, Cu-K α radiation source ($\lambda = 1.5406 \text{ \AA}$) and a Pilatus 300 K detector. The powder was sandwiched between two Kapton windows and measurements were performed with a sample to detector distance of 134 mm (WAXS) and 1080 mm (SAXS) between sample and detector, with an exposure time of 100 s. The q-range measured was determined with a calibration measurement of silver behenate and the 2D scattering patterns were azimuthally integrated to generate the 1D scattering curve. Transmission corrections as well as background corrections by the signal from an empty cell were performed.

Scanning SWAXS and SAXS tomography of the electrodes were performed at the cSAXS beamline (X12SA) at the Swiss Light Source, Paul Scherrer Institute (Switzerland). The *operando* experiment and *ex situ* tomography experiments were performed in two different experiments but using the similar setup. An X-ray beam (13.2 keV photon energy) was focused to a spot size of approximately 25 x 15 μm^2 . An evacuated flight tube was placed between the sample and the detectors to reduce air scattering and absorption. Scattering patterns were simultaneously measured using a Eiger 9M detector for SAXS in the *operando* experiment and a Pilatus 2M detector in the *ex situ* tomography experiment. A Pilatus 300kw detector oriented as a vertical strip were placed below the sample for WAXS. The sample to detector distance was approximately 2 m for SAXS and 0.6 m for WAXS. The q-ranges covered by the two detectors were determined with calibration measurements of silver behenate (SAXS) and lanthanum hexaboride (WAXS).

The samples were mounted on rotational and translational stages with the hard carbon electrode on the top to have free path for the scattered X-rays to reach the WAXS detector placed underneath, schematic Figure 1 and photographic images in Figure S1. Each scanning SWAXS image and the projections in the tomograms were scanned with a step size of 25 and 15 μm in the horizontal and vertical directions, respectively, using an exposure time of 0.1 s. For the tomograms 72 projections were measured. To confirm the absence of structural changes from radiation damage after a tomogram a projection at 0° rotation was measured before and after each tomogram, to ensure the same signals were retrieved from the two measurements, Fig S5.

Reconstruction of tomograms and data analysis

The two-dimensional scattering patterns were azimuthally integrated to retrieve one-dimensional scattering curves with the Matlab *cSAXS scanning SAXS package* developed by the CXS group, Paul Scherrer Institut (Switzerland)²⁷. To analyze the 2D images collected during *operando* sodiation the scattering data was divided in different q-regions where the scattering intensity was averaged in each pixel, generating 2D images with a contrast based on the scattering intensity in the different characteristic q-regions of the hard carbon structure as discussed in section 2, Fig 2. The current collector and surrounding electrolyte were masked out based on the transmission and scattering intensity in the range $q = 0.12 - 0.3 \text{ \AA}^{-1}$, where hard carbon scatter strongly. To visualize the spatial changes in scattering intensity during sodiation, difference maps between the intensity in the selected q-regions of the *operando* image (op #) and the pristine image were calculated, according to equation 1. The difference maps are created by subtracting the average intensity in the selected q-region of the pristine electrode from the intensity in the *operando* scans in each pixel and normalizing by the intensity from the pristine electrode to correct for thickness variations inherent in the 2D projections.

$$\text{Difference map} = \frac{\bar{I}_{op \#}^{\text{selected } q\text{-region}} - \bar{I}_{pristine}^{\text{selected } q\text{-region}}}{\bar{I}_{pristine}^{\text{selected } q\text{-region}}} \quad \text{eq. 1.}$$

To perform the tomographic reconstructions an iterative reconstruction algorithm developed by Liebi et. al.²⁸ was applied where the intensity of the scattering is optimized with the use of spherical harmonics as commonly applied for SAXS tensor tomography. The scattering curve was divided in 39 linearly spaced q-bins and the 2D scattering projections were transmission corrected and aligned using the scattering intensity in the range $q = 0.12 - 0.3 \text{ \AA}^{-1}$ ²⁹. The generated 3D SAXS tomograms were filtered using a mean 3D filter with a kernel of 2*2*2 pixels to smoothen noise in the visualisations. The homogeneity of the electrodes was compared by creating a histogram over the greyscale values of the chosen scattering intensities in the masked region of the electrode volume.

Acknowledgement

The authors acknowledge the Paul Scherrer Institute, Villigen PSI, Switzerland for provision of synchrotron radiation beamtime at the beamline cSAXS of the SLS. The work was performed in part at Chalmers Analysis Laboratory (CMAL). This work was supported by the Area of Advance Nano at Chalmers University of Technology through an excellence initiative PhD student position. We acknowledge Magnus Karlsteen at Chalmers University of Technology for assisting with 3D printing of sample holders for the experimental setup at cSAXS. LN, LR and ML received funding from the European Research Council Starting Grant MUMOTT (ERC-2020-StG 949301), funded by the European Union. MC and CA have received funding from the European Union's Horizon 2020 research and innovation programme under the Marie Skłodowska-Curie grant agreement No. 884104. Views and opinions expressed are however those of the author(s) only and do not necessarily reflect those of the European Union or the European Research Council Executive Agency. Neither the European Union nor the granting authority can be held responsible for them.

References

- (1) Dou, X.; Hasa, I.; Saurel, D.; Vaalma, C.; Wu, L.; Buchholz, D.; Bresser, D.; Komaba, S.; Passerini, S. Hard carbons for sodium-ion batteries: Structure, analysis, sustainability, and electrochemistry. *Materials Today* **2019**, *23*, 87-104.
- (2) Delmas, C. Sodium and sodium-ion batteries: 50 years of research. *Advanced Energy Materials* **2018**, *8* (17), 1703137.
- (3) Saurel, D.; Segalini, J.; Jauregui, M.; Pendashteh, A.; Daffos, B.; Simon, P.; Casas-Cabanas, M. A SAXS outlook on disordered carbonaceous materials for electrochemical energy storage. *Energy Storage Materials* **2019**, *21*, 162-173. DOI: 10.1016/j.ensm.2019.05.007.
- (4) Wen, Y.; He, K.; Zhu, Y.; Han, F.; Xu, Y.; Matsuda, I.; Ishii, Y.; Cumings, J.; Wang, C. Expanded graphite as superior anode for sodium-ion batteries. *Nature communications* **2014**, *5* (1), 4033.
- (5) Rodriguez-Palomo, A.; Lutz-Bueno, V.; Cao, X.; Kádár, R.; Andersson, M.; Liebi, M. In situ visualization of the structural evolution and alignment of lyotropic liquid crystals in confined flow. *Small* **2021**, *17* (7), 2006229.
- (6) Xie, F.; Xu, Z.; Guo, Z.; Titirici, M.-M. Hard carbons for sodium-ion batteries and beyond. *Progress in Energy* **2020**, *2* (4), 042002.
- (7) Simone, V.; Boulineau, A.; De Geyer, A.; Rouchon, D.; Simonin, L.; Martinet, S. Hard carbon derived from cellulose as anode for sodium ion batteries: Dependence of electrochemical properties on structure. *Journal of energy chemistry* **2016**, *25* (5), 761-768.
- (8) Stratford, J. M.; Kleppe, A. K.; Keeble, D. S.; Chater, P. A.; Meysami, S. S.; Wright, C. J.; Barker, J.; Titirici, M.-M.; Allan, P. K.; Grey, C. P. Correlating local structure and sodium storage in hard carbon anodes: insights from pair distribution function analysis and solid-state NMR. *Journal of the American Chemical Society* **2021**, *143* (35), 14274-14286.
- (9) Chen, X.; Tian, J.; Li, P.; Fang, Y.; Fang, Y.; Liang, X.; Feng, J.; Dong, J.; Ai, X.; Yang, H. An overall understanding of sodium storage behaviors in hard carbons by an “adsorption-intercalation/filling” hybrid mechanism. *Advanced Energy Materials* **2022**, *12* (24), 2200886.
- (10) Alvin, S.; Yoon, D.; Chandra, C.; Cahyadi, H. S.; Park, J.-H.; Chang, W.; Chung, K. Y.; Kim, J. Revealing sodium ion storage mechanism in hard carbon. *Carbon* **2019**, *145*, 67-81.
- (11) Xiao, B.; Rojo, T.; Li, X. Hard carbon as sodium-ion battery anodes: progress and challenges. *ChemSusChem* **2019**, *12* (1), 133-144.
- (12) Chen, X.; Liu, C.; Fang, Y.; Ai, X.; Zhong, F.; Yang, H.; Cao, Y. Understanding of the sodium storage mechanism in hard carbon anodes. *Carbon Energy* **2022**, *4* (6), 1133-1150.
- (13) Kim, H.; Hyun, J. C.; Kim, D. H.; Kwak, J. H.; Lee, J. B.; Moon, J. H.; Choi, J.; Lim, H. D.; Yang, S. J.; Jin, H. M. Revisiting Lithium-and Sodium-Ion Storage in Hard Carbon Anodes. *Advanced Materials* **2023**, *35* (12), 2209128.
- (14) Weaving, J. S.; Lim, A.; Millichamp, J.; Neville, T. P.; Ledwoch, D.; Kendrick, E.; McMillan, P. F.; Shearing, P. R.; Howard, C. A.; Brett, D. J. Elucidating the sodiation mechanism in hard carbon by operando raman spectroscopy. *ACS Applied Energy Materials* **2020**, *3* (8), 7474-7484.
- (15) Kitsu Iglesias, L.; Antonio, E. N.; Martinez, T. D.; Zhang, L.; Zhuo, Z.; Weigand, S. J.; Guo, J.; Toney, M. F. Revealing the Sodium Storage Mechanisms in Hard Carbon Pores. *Advanced Energy Materials* **2023**, *13* (44), 2302171.
- (16) Stevens, D.; Dahn, J. An in situ small-angle X-ray scattering study of sodium insertion into a nanoporous carbon anode material within an operating electrochemical cell. *Journal of The Electrochemical Society* **2000**, *147* (12), 4428.

- (17) Zhang, B.; Ghimbeu, C. M.; Laberty, C.; Vix-Guterl, C.; Tarascon, J. m. Correlation between microstructure and Na storage behavior in hard carbon. *Advanced Energy Materials* **2016**, *6* (1), 1501588.
- (18) Zhou, H.; Song, Y.; Zhang, B.; Sun, H.; Khurshid, I. A.; Kong, Y.; Chen, L.; Cui, L.; Zhang, D.; Wang, W. Overview of electrochemical competing process of sodium storage and metal plating in hard carbon anode of sodium ion battery. *Energy Storage Materials* **2024**, 103645.
- (19) Jian, Z.; Xing, Z.; Bommier, C.; Li, Z.; Ji, X. Hard carbon microspheres: potassium-ion anode versus sodium-ion anode. *Advanced Energy Materials* **2016**, *6* (3), 1501874.
- (20) Morikawa, Y.; Nishimura, S. i.; Hashimoto, R. i.; Ohnuma, M.; Yamada, A. Mechanism of sodium storage in hard carbon: an X-ray scattering analysis. *Advanced Energy Materials* **2020**, *10* (3), 1903176.
- (21) Härk, E.; Ballauff, M. Carbonaceous materials investigated by small-angle X-ray and neutron scattering. *C* **2020**, *6* (4), 82.
- (22) Lübke, E.; Helfen, L.; Cook, P.; Mirolo, M.; Vinci, V.; Korjus, O.; Fuchsichler, B.; Koller, S.; Brunner, R.; Drnec, J. The origins of critical deformations in cylindrical silicon based Li-ion batteries. *Energy & Environmental Science* **2024**.
- (23) Stevens, D.; Dahn, J. The mechanisms of lithium and sodium insertion in carbon materials. *Journal of The Electrochemical Society* **2001**, *148* (8), A803.
- (24) Xie, F.; Xu, Z.; Jensen, A. C.; Ding, F.; Au, H.; Feng, J.; Luo, H.; Qiao, M.; Guo, Z.; Lu, Y. Unveiling the role of hydrothermal carbon dots as anodes in sodium-ion batteries with ultrahigh initial coulombic efficiency. *Journal of Materials Chemistry A* **2019**, *7* (48), 27567-27575.
- (25) Härk, E.; Petzold, A.; Goerigk, G.; Ballauff, M.; Kent, B.; Keiderling, U.; Palm, R.; Vaas, I.; Lust, E. The effect of a binder on porosity of the nanoporous RP-20 carbon. A combined study by small angle X-ray and neutron scattering. *Microporous and Mesoporous Materials* **2019**, *275*, 139-146.
- (26) Youn, Y.; Gao, B.; Kamiyama, A.; Kubota, K.; Komaba, S.; Tateyama, Y. Nanometer-size Na cluster formation in micropore of hard carbon as origin of higher-capacity Na-ion battery. *npj Computational Materials* **2021**, *7* (1), 48.
- (27) CXS group Scanning SAXS Software Package, P., Switzerland, Available from: <https://www.psi.ch/en/sls/csaxs/software> .
- (28) Liebi, M.; Georgiadis, M.; Kohlbrecher, J.; Holler, M.; Raabe, J.; Usov, I.; Menzel, A.; Schneider, P.; Bunk, O.; Guizar-Sicairos, M. Small-angle X-ray scattering tensor tomography: Model of the three-dimensional reciprocal-space map, reconstruction algorithm and angular sampling requirements. *Acta Crystallographica Section A: Foundations and Advances* **2018**, *74* (1), 12-24.
- (29) Guizar-Sicairos, M.; Thurman, S. T.; Fienup, J. R. Efficient subpixel image registration algorithms. *Optics letters* **2008**, *33* (2), 156-158.